ACS APPLIED ENERGY MATERIALS

www.acsaem.org Article

Air-Stable Hybrid Perovskite Solar Cell by Sequential Vapor Deposition in a Single Reactor

Siphelo Ngqoloda, Christopher J. Arendse,* Theophillus F. Muller, Paul F. Miceli, Suchismita Guha, Louise Mostert, and Clive J. Oliphant

Cite This: *ACS Appl. Energy Mater.* 2020, 3, 2350−2359 Read Online

ACCESS | Metrics & More | Article Recommendations | Supporting Information

ABSTRACT: We demonstrate a facile two-step low-pressure vapor deposition of methylammonium lead iodide ($MAPbI_3$) perovskite films in a single reactor. Continuous, polycrystalline lead iodide (PbI_2) films were deposited in the first step and successfully converted to high quality perovskite films in the second step during exposure of PbI_2 films to methylammonium iodide (MAI) vapor. A complete conversion was realized after 90 min of exposure with an average grain size of 3.70 ± 1.80 μm. The perovskite conversion starts at the PbI_2 surface through the intercalation reaction of PbI_2 and MAI vapor molecules and progresses toward the PbI_2/substrate interface. The coverage and quality of the perovskite thin film are controlled by that of the predeposited PbI_2 film. The absorbance measurements confirmed air stability of the fully converted perovskite for 21 days, ascribed to its superior morphology and grain size. Finally, a planar single-junction perovskite solar cell with no additives or additional interfacial engineering was fabricated and tested under open-air conditions, yielding a best power conversion efficiency of 11.7%. The solar cell maintains 85% of its performance up to 13 days in the open air with a relative humidity up to 80%.

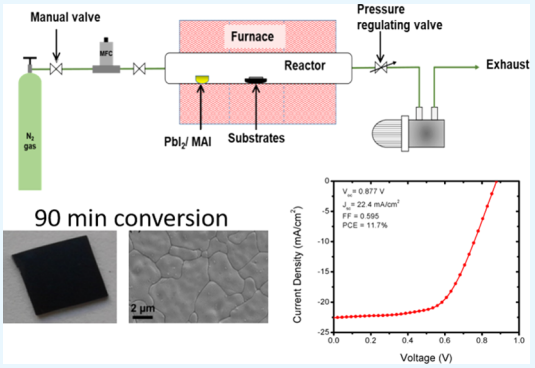

KEYWORDS: *two-step vapor deposition, large grains, intercalation, air-stable, planar device*

INTRODUCTION

Organic−inorganic hybrid perovskites have emerged as an interesting class of semiconductor materials for their application in photovoltaic (PV) and other semiconducting devices.[1−3] The first application of perovskites in PV technology was in 2009 by Kojima and co-workers,[4] with measured power conversion efficiency (PCE) of about 3.8% and in 2012 by Lee et al.[5] with an improved PCE of about 10.9%. A fast rise in PCE of this material observed in a decade from 3.8% to 25.2% is highly unique compared to other established PV technologies such as c-Si, GaAs, CdTe, and organic-based solar cells.[6] The high efficiency of these organic metal halide perovskites has been attributed to its excellent optical and electronic properties. These include high optical absorption coefficient (ca. 10^4 cm^{-1}) and a wide range of visible absorption with tunable direct band gap (1.5−2.3 eV), long carrier diffusion lengths, ambipolar charge transport, low intrinsic recombination rates due to weakly bounded excitons, high crystallinity, and low-temperature processing.[3,7] However, hybrid perovskite absorbers still face the issue of chemical instability as they degrade under continued exposure to moisture, light illumination, and UV light and are unstable at high temperatures.[1,3,7]

Perovskite thin films are usually deposited via three main routes: solution spin-coating, physical vapor deposition (vacuum thermal evaporation), and chemical vapor deposition (CVD). All these methods are either single-step, where the organic cation is deposited simultaneously with the metal halide, or two-step sequential deposition, with the metal halide predeposited and organic halide material introduced in the second step.[8−14] The spin-coating methods have several challenges, which include incomplete surface coverage, use of solvents that may promote high instability, processing in inert environments, and lack of reproducibility. Thermal evaporation, on the other hand, requires the use of dedicated ultrahigh-vacuum systems. In addition, these techniques are not easily scalable and are in most cases incompatible with traditional deposition methods used in the semiconductor industry.

CVD has the advantage of being a well-established technique in the silicon processing industry.[15] It allows for the deposition of uniform thin films onto large substrate sizes, which aids in the scalability of the perovskite deposition process. CVD has been employed for the deposition of hybrid perovskite thin

Received: September 29, 2019
Accepted: February 11, 2020
Published: February 11, 2020

https://dx.doi.org/10.1021/acsaem.9b01925
ACS Appl. Energy Mater. 2020, 3, 2350−2359

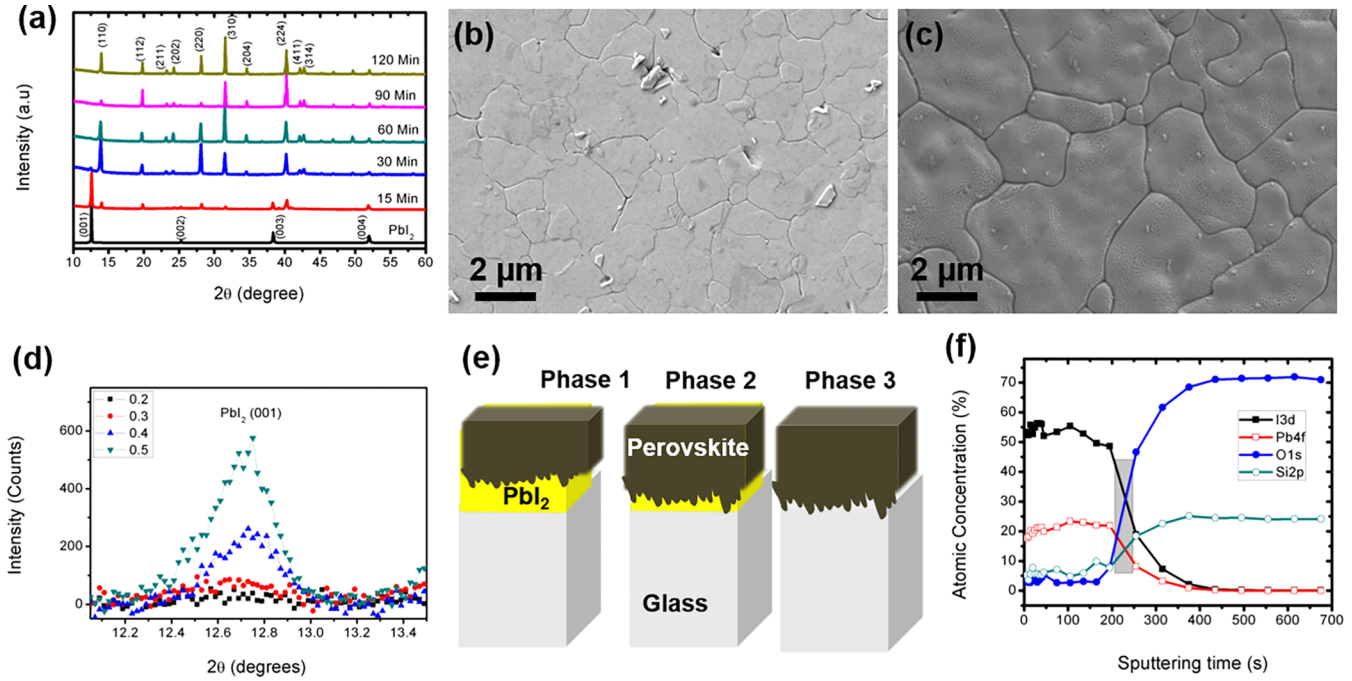

Figure 1. (a) XRD patterns of PbI_2 film (bottom) and the subsequent converted perovskite samples: 15, 30, 60, 90, and 120 min from bottom to top patterns. (b) Planar SEM micrograph of the as-deposited PbI_2 thin film and (c) 90 min converted perovskite film, both on glass substrate showing smooth and flat grains. (d) Grazing incident XRD pattern of the 30 min converted sample at different angles for the PbI_2 peak position. (e) Schematic illustration of the perovskite conversion mechanism. (f) XPS depth profile of the 90 min converted perovskite sample showing the atomic concentration depth profile.

films by various groups based on the one-step[16] and two-step processes.[14,15,17−26] Although simpler, during one-step CVD it may be difficult to control the coevaporation of the sources, which results in poor conversion and film quality. The two-step CVD method, termed hybrid CVD (HCVD), requires the predeposition of the Pb halide on substrates typically by spin-coating or thermal evaporation.[15,17−26] The predeposited Pb halide thin films are then placed inside the CVD furnace a distance away from the methylammonium iodide (MAI) source that is vaporized by thermal heating. The resultant MAI vapors are transported by the inert gas that diffuse through the layered Pb halide structure, forming a solid perovskite during a chemical reaction of the MAI molecules with the layered Pb halide.[15,17] HCVD still poses a challenge to scalability of the CVD technique, since the predeposited Pb halide layers are dependent on the inherent constraints of the spin-coating or thermal evaporation techniques. The highest PCE of a hybrid perovskite-based solar cell fabricated by HCVD method is 18.9%, where the PbI_2 layer was deposited by spin-coating.[27] A comparison of various deposition techniques and the issue of scalability of perovskite films are found in a recent review by Swartwout et al.[28] and Luo et al.[29] with PCE ranging between 7.9 and 18.9%.

The major drawback of perovskites is its instability when exposed to humidity, particularly for those grown by spin-coating, which requires the devices to be processed in a glovebox. There is thus a need to improve the stability of perovskites by producing thin films with large grain sizes, full surface coverage, and improved morphology, while maintaining a high throughput on large-area substrates. Several strategies such as interface engineering, addition of interfacial coating layers to protect against moisture permeation, encapsulating layers to shield against moisture, and doping of the perovskite absorber layer have been employed to improve the solar cell stability. Among solution-processed films, the use of ionic additives degrades the performance of encapsulated perovskite solar cells by only 5% under continuous simulated full spectrum sunlight for more than 75 days at elevated temperatures.[30] Air stability still remains an issue, and there are not many reports of stability tests found in the literature from unencapsulated CVD grown perovskite solar cells. Wang et al.[20] investigated the stability of CVD perovskite devices, which remained stable for 100 days stored in air at a relative humidity of 40%. However, the group used a fresh hole transport layer and metal contact for each measurement. Peng et al.[21] also reported on the stability of their perovskite solar cell, which maintained 80% of initial performance after 31 days stored at ambient environment with 30% relative humidity. Another study of CVD grown perovskite device stability was reported by Tran et al.[26] where they employed single-wall carbon nanotubes as a counter electrode, and their device maintained 80% of the initial 7.9% efficiency for 500 h of test under an ambient atmosphere. Furthermore, Pammi et al.[31] investigated long-term stability of CVD grown perovskite films on glass, but these investigations were not conducted on a functioning device. Shallcross et al.[32] also report on the vapor growth of the hybrid perovskite films and the role of the interfacial TiO_2 surface defects on the perovskite stability but show no application of vapor-deposited perovskite films in solar cells. A recent study utilized a fast vapor deposition technique in a custom-built reactor, enabling cost-effective scalable manufacturing.[33] A 6.9% PCE was achieved in this study, and no long-term stability measurements were conducted. Recently reported deposition methodologies to increase the PCE of vapor-deposited perovskite solar cells include white-light illumination assisted deposition,[34] vapor

https://dx.doi.org/10.1021/acsaem.9b01925
ACS Appl. Energy Mater. 2020, 3, 2350−2359

exchange deposition,[35] and vapor assisted solution processing.[36] To reduce the production and installation cost of $MAPbI_3$ perovskite solar panels, the emphasis should be on addressing and improving the intrinsic stability of the $MAPbI_3$ perovskite absorber layer, as this will remove the costly and stringent encapsulation process required to protect the perovskite solar cell from humidity.

In this contribution, we report on the vapor deposition of a PbI_2 thin film in a CVD reactor, followed by its conversion to a uniform, polycrystalline $MAPbI_3$ perovskite thin film, using the same CVD reactor. The novelty of this approach stems from the deposition of a uniform, compact, and crystalline PbI_2 layer in the same CVD reactor at low pressure, as opposed to other hybrid CVD methods where the PbI_2 layer is deposited by either spin-coating or high-vacuum thermal evaporation in a different reactor. As the CVD reactor allows for independent control of deposition parameters, this technique aids in improving the reproducibility of the perovskite thin films with enhanced morphology and stability. Moreover, since the deposition of the uniform PbI_2 layer is performed in the same CVD reactor in the first step, a scale-up synthesis is facilitated. We further investigate the perovskite conversion process by exposing PbI_2 films to the MAI vapors in the second conversion step. The structural, morphological, and compositional properties are probed by powder and grazing incidence X-ray diffraction (XRD), scanning electron microscopy (SEM), and X-ray photoelectron spectroscopy (XPS), respectively. Furthermore, the air stability of a fully converted perovskite thin film is investigated through absorbance measurements for 21 days. The optimum converted perovskite film is applied in a planar solar cell architecture with the best PCE of 11.7%, measured in air. The solar cell maintained 85% of its performance for 13 days of measurements under ambient conditions with the temperature ranging from 15 to 22 °C and the relative humidity ranging from 60 to 80%.

RESULTS AND DISCUSSION

Thin Film Deposition. Crystalline PbI_2 thin films were successfully deposited in the first vapor deposition step. Figure 1a shows the XRD pattern of a pure, high quality PbI_2 thin film on glass substrate, depicting its polycrystalline nature. The observed peaks at ∼12.74°, 25.59°, 38.76°, and 52.51° belong to the (001), (002), (003), and (004) diffracting planes, respectively, based on the Joint Committee on Powder Diffraction Standards (JCPDS, data no. 07-0235). This XRD pattern is indexed to the hexagonal ($P\bar{3}m1$) structure[37,38] of a highly crystalline PbI_2 film. A slight shift in 2θ-peak positions was observed as compared to the standard pattern, which suggest a slight compression of the *d*-spacing (<1%) and hence compression of the *c*-axis lattice constant that can be ascribed to the higher growth temperature (ca. 380 °C) of the PbI_2 films. The (001) peak is the most intense, indicating a preferred growth orientation along the [001] direction, which is parallel to the *c*-axis of the hexagonal crystal structure. This preferred growth direction is linked to the growth mechanism of PbI_2 thin films, which follows a layer-by-layer growth of repeating I−Pb−I monolayers along the *c*-axis and separated by a van der Waals gap.[37−39] This van der Waals gap allows an easy intercalation of foreign molecules, such as MAI, during the conversion to perovskite.

A uniform, smooth PbI_2 film is shown in the SEM micrograph in Figure 1b with large and compact grains visible with well-defined grain boundaries. This successful growth of a PbI_2 film is achieved through evaporation of PbI_2 source that moves toward the substrate due to the temperature gradient in the tube assisted by N_2 flow. The growth begins with this layer-by-layer deposition on the substrate forming a continuous film under the optimum conditions of temperature and pressure. The smooth surface is related to the grain formation during deposition (layer-by-layer growth), and these flat grains of PbI_2 are often termed platelet grains.[14,37−39] The SEM micrograph also confirms a full surface coverage with no pinholes present in the film. Optical micrographs are provided in the Supporting Information (Figure S2). The lateral grain size amounts to 1.60 ± 0.62 μm (as measured from the SEM micrograph, Figure 1b). There are, however, grains larger than 1.6 μm measured along their length. The PbI_2 large grain sizes are due to a fast-preferred grain growth along the lateral direction where there is a minimized facet surface energy as opposed to along the *c*-axis (vertical direction).[39] Hence, the grains are larger than the film thickness of 230 ± 15 nm. These larger grains are favorable for conversion to perovskite and are expected to grow larger in size during the perovskite conversion through the diffusion of MAI molecules.

The PbI_2 thin film was successfully converted into the $MAPbI_3$ perovskite film during exposure to the MAI vapors. During conversion, the MAI vapors diffuse toward the heated PbI_2 substrates, which upon contact with the PbI_2 surface diffuse through its layered framework. The proposed reaction mechanism is an intercalation of the MAI into the layered PbI_2, beginning at the surface (top)[10] or at the substrate interface (bottom).[17] Here the deposition mechanism and conversion process are investigated at different conversion times. Figure 1a shows the XRD patterns of $MAPbI_3$ perovskites converted after 15, 30, 60, 90, and 120 min exposure times. The $MAPbI_3$ pattern shows major diffraction peaks at 14.05°, 19.94°, 28.39°, 31.81°, and 40.61° 2θ, assigned to the (110), (112), (220), (310), and (224) planes, respectively, of the tetragonal (*I*4/*mcm*) $MAPbI_3$ phase known to be stable at room temperature.[40,41] There are other smaller peaks at 23.44° (211), 24.42° (202), 34.91° (204), and 43.09° (330), also indexed to tetragonal $MAPbI_3$ perovskite. The small peak at 23.44° is inconsistent with the cubic symmetry of $MAPbI_3$, hence confirming a pure tetragonal phase perovskite.[40,41] The XRD pattern of the 15 min converted film shows sharp peaks belonging to the hexagonal PbI_2 phase that is more intense than the $MAPbI_3$ perovskite peaks, which confirms the coexistence of the two phases. This demonstrates that the conversion process is incomplete after 15 min. A small peak at 12.74° that belongs to a low level PbI_2 impurity appears for the 30 and 60 min converted perovskites (as seen in Figure 1a), suggesting that the majority of the PbI_2 is converted to perovskite with a small fraction of PbI_2 still present. The PbI_2 diffraction peak disappears after 90 min conversion time, confirming complete conversion of the PbI_2 film into $MAPbI_3$ perovskite after this exposure time. Further exposure after 120 min does not induce an appreciable change in the XRD pattern. These results show that the intercalating reaction begins the instant that the PbI_2-coated substrate is exposed to the MAI vapor.

The morphology of the polycrystalline perovskite thin films was investigated by means of SEM as shown in Figure 1c and in the Supporting Information (Figure S3a−d). Low surface coverage, pinholes, and inhomogeneity of the perovskite thin film often results in poor solar cell performance.[13] An advantage of a two-step deposition process, especially in this

https://dx.doi.org/10.1021/acsaem.9b01925
ACS Appl. Energy Mater. 2020, 3, 2350−2359

instance, is that the predeposited PbI_2 morphology can be controlled carefully, resulting in high quality perovskite thin films. The yellow PbI_2 film was converted into a dark brown/black perovskite upon exposure to the MAI vapor during the second step of the sequential deposition where even the partially converted 15 min sample appears dark. The optical micrographs of the converted perovskite films show uniform and continuous films with full surface coverage for all conversion times. The perovskite film obtained after 90 min, which is the fully converted sample, shows visible grains of sizes up to 6 μm in the optical micrograph. Details of film morphology are included in the Supporting Information.

It is known that the grain sizes and shapes of PbI_2 change after conversion to perovskites due to the insertion of the MAI molecule within its layered structure.[10,15,17] The lattice parameter along the *c*-axis expands upon conversion of the hexagonal PbI_2 (c = 6.95 Å) to tetragonal $MAPbI_3$ (c = 12.44 Å), and hence the volume of the converted perovskite increases as compared to that of PbI_2.[14] After 15 min conversion time, the grains observed from the SEM micrograph (Figure S3a) are well-defined with clear grain boundaries, average grain size of 0.73 ± 0.24 μm, and smaller in size compared to that observed for the PbI_2 film. With prolonged conversion time up to 30 and 60 min, the grain size increases to average values of 1.02 ± 0.58 and 1.61 ± 0.77 μm, respectively, as shown in Figure S3b,c and comparable to those measured for the PbI_2 film. However, the grains appear rougher and irregular. Larger and flatter grains are observed after 90 min conversion with average size of 3.70 ± 1.80 μm (Figure 1c), followed by grain-coarsening and size reduction after 120 min conversion to 2.36 ± 1.03 μm (Figure 3Sd). The grain size evolution is summarized in Table 1.

Table 1. Grain Size, RMS Roughness, Thickness, and Pb/I Ratio by EDS for Different Conversion Times

conversion time (min)	grain size (μm)	RMS roughness (nm)	thickness (nm)	Pb/I ratio
0 (PbI_2 layer)	1.60 ± 0.62	8.5	230	0.58
15	0.73 ± 0.24	45.7	405	0.43
30	1.02 ± 0.58	39.8	409	0.36
60	1.61 ± 0.77	33.5	415	0.37
90	3.70 ± 1.80	32.7	450	0.36
120	2.36 ± 1.03	51.9	444	0.37

The RMS roughness extracted from the AFM micrographs of the perovskite thin film reduces from 45.7 nm after 15 min conversion to 32.7 nm after 90 min conversion, followed by an increase to 51.9 nm after 120 min conversion (see Table 1 and Figure S4f–j). There is an inverse relationship between the grain size and roughness, which suggests that the grain growth results in a continuous and smooth film. The increase in RMS roughness from predeposited PbI_2 thin films to the perovskite films is due to the insertion of the MAI molecule within the layered network of PbI_2 where the perovskite grain formation induces surface roughness. The difference in morphology was also observed in the SEM micrographs with perovskite films depicting defined grains (Figure 1c) as compared to the flat grains of PbI_2 (Figure 1b). The 90 min sample had a relatively smaller roughness (32.7 nm) than the other perovskite samples, which confirms the smoother and larger grains observed in the SEM micrographs (Figure 1c). The larger grain size and smoother surface of the 90 min sample are attributed to the complete conversion, presenting the saturation stage of this sequential deposition process. It should be noted that the large grain size and low RMS roughness observed after 90 min conversion were not observed for any CVD prepared perovskite and without any postdeposition annealing. Pinholes and grain boundaries are defect centers that impede the electron−hole transport, inducing carrier recombination sites and deteriorating device performance.[42,43] The cross-sectional SEM micrograph of our CVD grown perovskite film shows continuous, columnar grains along the film thickness with no grain boundaries parallel to the substrate (Figure S3e), which is beneficial for efficient charge transport. The superior grain sizes reported here suggest a reduced defect density, which as we see later contributes toward the improved stability and performance of the devices.

The changes in the grain shapes and sizes are related to the deposition kinetics. The unit cell volume of hexagonal PbI_2 is about 0.1255 nm^3 at room temperature, and that of cubic $MAPbI_3$ is about 0.2475 nm^3 at 85 °C,[41] almost double that of PbI_2 ($MAPbI_3$ were deposited at 180 °C). This grain morphology evolution suggests that during the initial stages (15 min) of the conversion process the larger grains of PbI_2 shrink and separate during the MAI intercalation into the layered PbI_2, resulting in smaller, partially converted perovskite grains. With further MAI exposure and subsequent intercalation, the grain size increases due to volume expansion as more PbI_2 is converted to perovskite. The maximum grain size observed after 90 min of conversion and the subsequent reduction thereof after 120 min suggest that the intercalation stops and that the saturation stage of the perovskite conversion is achieved after 90 min. With all the PbI_2 converted to perovskite, the grain growth stops, and the films appear to oversaturate after 120 min conversion, resulting in grain size reduction and coarsening. The 120 min sample remained exposed to MAI vapor after the saturation stage, but no signature of MAI residue was observed in the XRD pattern (Figure 1a) in which MAI diffraction peaks normally appear at 9.84°, 19.74°, and 29.79°.[44] The absence of crystalline MAI confirms that an MAI layer did not form after full conversion. The reduction in the grain size is attributed to the coarsening of the grains that may be due to the unstable crystallization of the perovskite after full conversion of the PbI_2. This may be caused by the formation of an amorphous intermediate phase due to the oversupply of MAI vapors into the grains.[45] Furthermore, prolonged heat supply may then transform the crystalline structure into a thermodynamically stable phase.[19] The thickness of the PbI_2 layer and the converted perovskite samples are summarized in Table 1. The thickness of the fully converted sample (90 min with 450 nm) is approximately double that of the PbI_2 layer (230 nm), which agrees with previous reports and accords with the expected volume changes induced during the conversion process.[41,46]

The XRD pattern of the 15 min sample (Figure 1a) showed strong diffraction of the (110), (220), and (224) peaks, as inferred from the peak intensities, suggesting a mixed preferred orientation, which apparently arises from the volume expansion and the competing steric constraints in the reacted film. Extending the conversion time to 30 min resulted in the (110) and (220) being the preferred orientation with larger average grain size than the 15 min sample. The 60 and 120 min samples are highly orientated along the (310) planes with even larger grain sizes and a similar morphology as seen from their SEM micrographs (Figure S3c,d). Lastly, the 90 min exposed

https://dx.doi.org/10.1021/acsaem.9b01925
ACS Appl. Energy Mater. 2020, 3, 2350−2359

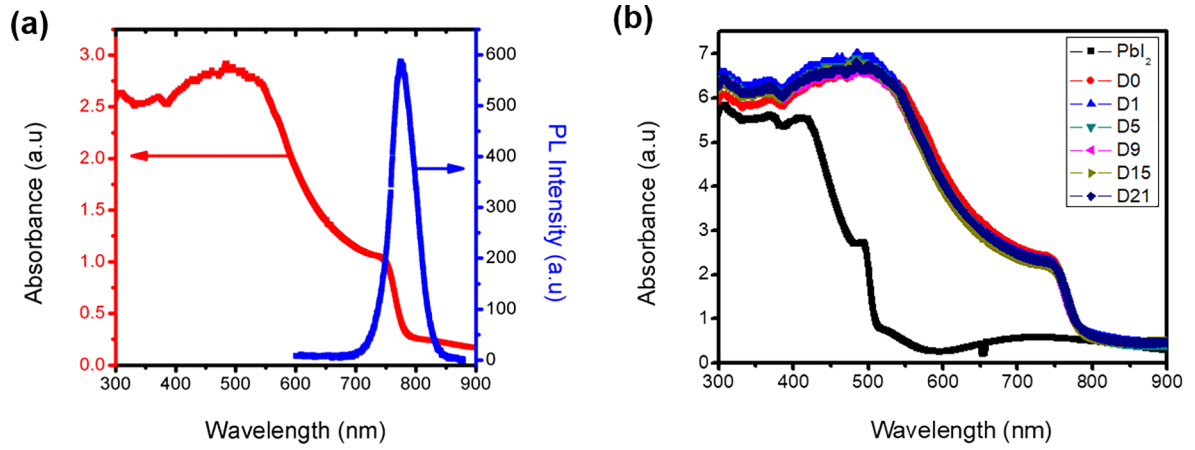

Figure 2. (a) Absorbance and photoluminescence spectra of the 90 min converted perovskite and (b) evolution of the absorbance spectra of the same sample measured for 21 days at ambient room conditions to probe film air stability.

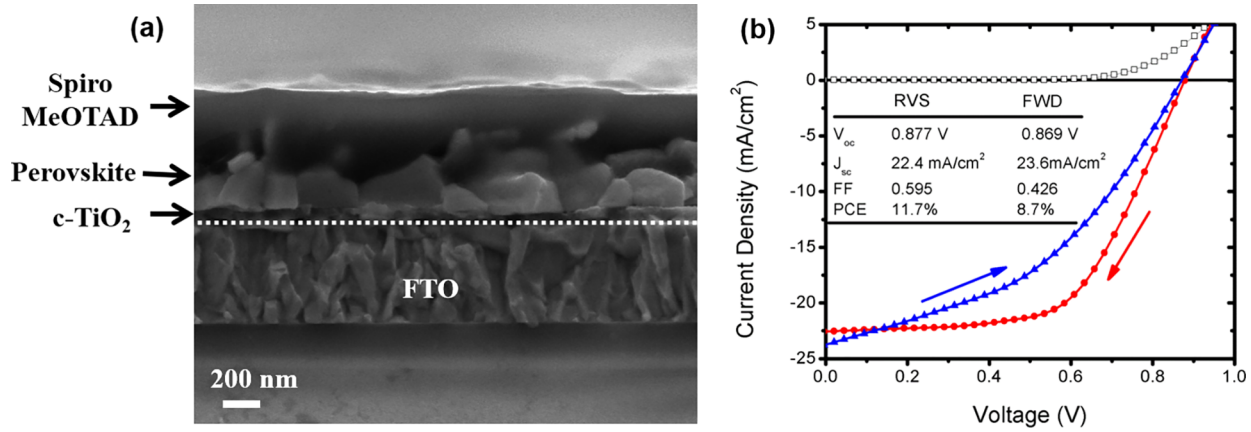

Figure 3. (a) SEM cross-sectional view of the 90 min perovskite solar cell showing all the layers except the metal contact. (b) *J*–*V* characteristic scanned in forward and reverse also showing the respective device parameters and performance.

sample has the largest grain size and different orientation along the (224) planes with well-suppressed (110) and (220) orientations shown in Figure 1a. These results suggest that larger grains of perovskites, obtained after 90 min conversion, do not grow along the (110) and (220), which is preferred orientation for grains <1 μm.[10,13,17]

During the conversion process, the MAI intercalates slowly through the layered PbI_2 framework and chemically reacts with the PbI_2, which subsequently transforms to solid $MAPbI_3$. However, this process is time-dependent, as the reaction does not happen simultaneously throughout the film thickness. As the exposure time is prolonged, more of the PbI_2 is converted to perovskite (30 and 60 min) until the entire film is completely converted (90 min). To gauge the presence of PbI_2 through the thickness of the film, grazing incident XRD (GIXRD) was performed on the 30 min sample, which had a small PbI_2 peak during normal XRD. GIXRD was probed at different grazing incident angles (0.2°, 0.3°, 0.4°, and 0.5°) as shown in Figure 1d to investigate the conversion process. As a note, low grazing incident angles probe the top surface, and higher angles penetrate deeper in the film. The low grazing angle (0.2°) shows no PbI_2 peak, suggesting an absence of PbI_2 on the film surface compared to high grazing angles (0.4° and 0.5°) where the PbI_2 peak appears, suggesting a presence of PbI_2 toward the bottom of the perovskite film. These results confirm that the perovskite conversion reaction starts at the PbI_2 surface and continue downward toward the substrate. This is in agreement with the proposed perovskite conversion mechanism by Chen et al.[10] The schematic illustration in Figure 1e shows the different phases of conversion: phase one with a high concentration of PbI_2 (15 min conversion), phase two with a small amount of PbI_2 at the bottom (30 and 60 min conversion), and finally phase three with a full consumption of PbI_2 (90 min).

X-ray photoelectron spectroscopy (XPS) was used to probe the atomic concentration depth profile of the 90 min perovskite film through sputtering with energetic argon ions, and the profile is shown in Figure 1f. Details of the XPS data are included in the Supporting Information (Figure S5). The Pb and I concentrations are higher on the surface (as expected) and are relatively constant throughout the film thickness, which then decreased toward the glass substrate–film interface, signified by the increased silicon and oxygen atomic concentrations. This substrate–film interface is marked with a rectangle in Figure 1f and found between 200 and 250 s of sputtering based on the abrupt reduction of lead and iodide profiles accompanied by an increase in silicon and oxygen concentrations (from the substrate). The presence of oxygen and silicon on the surface might be due to sample oxidation and contamination during handling and storage.

The optical behavior of the 90 min converted sample was investigated by absorbance and photoluminescence (PL)

https://dx.doi.org/10.1021/acsaem.9b01925
ACS Appl. Energy Mater. 2020, 3, 2350–2359

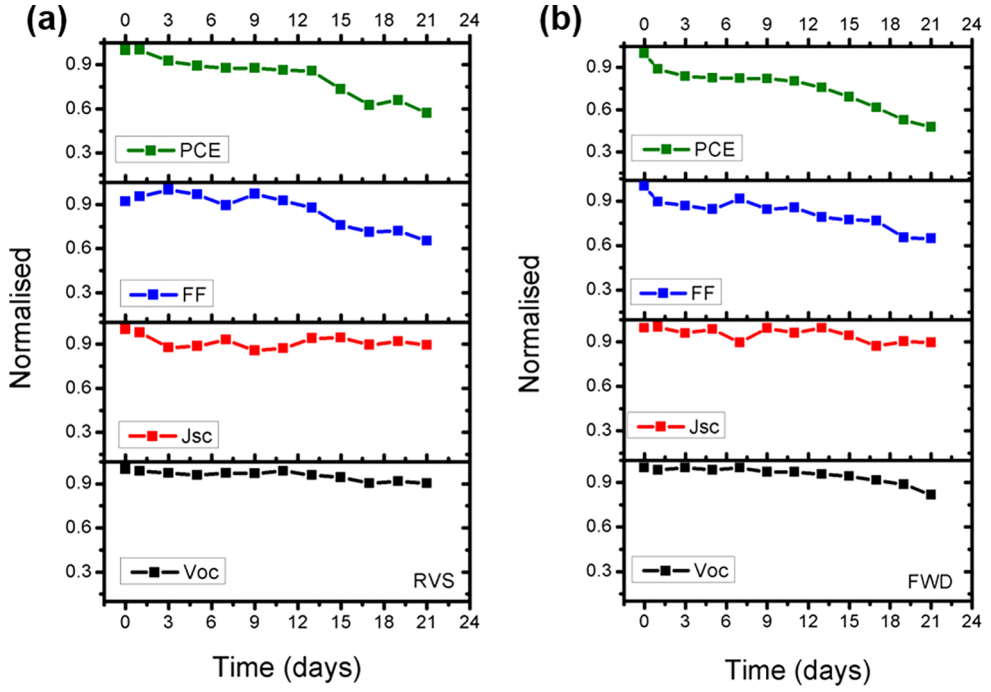

Figure 4. Evolution of the normalized open-circuit voltage (V_{oc}), short-circuit current density (J_{sc}), fill factor (FF), and the power conversion efficiency (PCE) of the device measured for 21 days in the (a) reverse and (b) forward scan.

spectroscopy, shown in Figure 2a. The perovskite film absorbs throughout the visible range with a sharp reduction at about 750 nm. This wide absorption confirms the high quality of sequential vapor grown perovskite films. The steady-state PL shows an intense peak at about 775 nm (1.59 eV), which agrees with the known $MAPbI_3$ perovskite optical band gap of 1.5−1.6 eV.[47,48] Details of the absorbance and extracted optical properties are provided in the Supporting Information.

After initial characterization, the absorbance spectra were measured daily on the fully converted (90 min) perovskite sample to investigate the air stability of the films. Samples were placed in the dark with uncontrolled ambient conditions (temperature and humidity). Temperatures during the measured days ranged from 15 to 22 °C and relative humidity from 60 to 80%. Figure 2b shows the evolution of the absorbance spectra of the 90 min perovskite sample. The film remained stable for 21 days of measurements, with slight changes in absorbance associated with the inhomogeneity of the sample thickness. The stability of the fully converted sample is due to its superior grain size and crystalline quality that is concomitant with a reduced defect density. Furthermore, the purity and compactness of these CVD deposited films with no pinholes to trap moisture and the absence of solvents in both deposition steps also contribute to its prolonged stability.

Device Performance and Stability. The 90 min converted sample with larger grain size was subsequently used as the absorber layer in the solar cells. The corresponding cross section of the planar perovskite solar cell device is shown in Figure 3a with FTO coated on glass followed by a double-spin-coated c-TiO_2 film as an electron transport layer, then the $MAPbI_3$ perovskite, and finally a layer of Spiro MeOTAD as hole transport material. The device was prepared in open air (without the use of a glovebox) and finalized by depositing a 100 nm Ag layer as back-contact.

The solar cells were characterized by current and voltage measurements under simulated AM 1.5G (100 mW/cm^2) solar irradiation in air, scanned in both forward and reverse. The current density (J)−voltage (V) curve is shown in Figure 3b for both forward and reverse scans, indicated with arrows. As shown, the device had an open circuit voltage (V_{oc}) of 0.869 V, short-circuit current density (J_{sc}) of 23.6 mA/cm^2, fill factor (FF) of 0.426, and power conversion efficiency (PCE) of 8.7% under forward scan. There is a hysteresis between forward and reverse sweeps. The reverse scan showed a better performance: V_{oc} = 0.877 V, J_{sc} = 22.4 mA/cm^2, FF = 0.595, and PCE = 11.7%. The most probable cause for hysteresis in our devices is due to ion migration, ferroelectric polarization, and charge accumulation at the c-TiO_2/perovskite interface.[49−51] Charge trapping at this interface lowers both FF and V_{oc}. Doping of the c-TiO_2 layer[52,53] and interface engineering[54] are normally employed as a means to increase the TiO_2 conductivity, improving the performance, and reducing the hysteresis of the device. Here we did not perform any c-TiO_2 doping, as the objective was to determine the applicability of a two-step CVD grown perovskite film for solar cell application. Future studies will entail the optimization of the individual non-perovskite layers and detailed quantum efficiency measurements.

Although the device showed hysteresis, we tested its performance stability since the film was stable under ambient room conditions. The devices were kept in the dark under ambient room conditions with temperature ranging between 15 and 22 °C and relative humidity ranged between 60 and 80%. Figure 4a,b shows the evolution of the V_{oc}, J_{sc}, FF, and PCE in reverse and forward scans as a function of time. These values were divided by the values obtained on day 1. V_{oc} remained above 90% throughout the measured period under reverse scan, and the minimum J_{sc} was 87%, fluctuating between this value and 99% (both in Figure 4a). A similar trend was observed at forward scan, except for a fast drop in V_{oc} during the final 2 days of measurements to about 80%

https://dx.doi.org/10.1021/acsaem.9b01925
ACS Appl. Energy Mater. 2020, 3, 2350−2359

(Figure 4b). The FF and the corresponding PCE were maintained at above 85% of their highest values for the first 13 days in the reverse sweep and then dropped significantly (Figure 4a). A steady drop in FF and PCE was observed for the forward sweep as shown in Figure 4b. The data values of the stability and the corresponding $J-V$ curves measured on consecutive days are provided in the Supporting Information (Figures S7 and S8).

The drop in device performance is attributed to the possibility of ion migration, which inhibits charge transport at the layer interfaces (electron and hole transport layers). Another possible reason could be the corrosion of the Ag contacts, which appeared as early as day 9 of measurements with a brownish color around its edges and regions in contact with the FTO. The corrosion of Ag metal reduces its conductivity and creates a high series resistance in the device.

CONCLUSIONS

We have demonstrated the deposition of pure, highly crystalline, smooth, and compact $MAPbI_3$ perovskite films on glass substrates by using a sequential vapor deposition method at low pressures in a single reactor. The as-deposited PbI_2 films grown in the first step were successfully converted to $MAPbI_3$ perovskite during their exposure to MAI vapor in the second step by using the same CVD reactor. The conversion begins at the surface and progresses toward the glass substrate, resulting in tetragonal $MAPbI_3$ perovskites. A growth in grain size was realized as the conversion time increases up to 90 min, where conversion saturation was observed with a grain size of 3.70 ± 1.80 μm. A perovskite-rich film was confirmed from the XPS depth profile. The fully converted perovskite film (90 min) was found to be optically stable in air with a high relative humidity up to 80% for more than 21 days. This stability is ascribed to its superior grain size, crystalline quality, high purity, and compactness of the film. Air-processed planar perovskite solar cell devices under similar ambient room conditions were achieved. The best device performance achieved was 11.7%, albeit with a hysteresis. After 13 days of exposure to high relative humidity, 85% of its initial PCE was maintained. This work opens a path toward a low-cost, scalable deposition technique for the manufacturing of air-stable hybrid alkali halide perovskite solar panels.

EXPERIMENTAL METHODS

Perovskite Film Fabrication. Corning glass substrates were cut into 1 cm × 1 cm sizes and subsequently cleaned in acetone and isopropanol for 10 min each in an ultrasonic bath and repeatedly rinsed with deionized water. The CVD system used in this study is composed of a horizontal ceramic tube, enclosed by a three-zone ceramic tube furnace (Brother XD 1600MT manufactured by Zhengzhou Brother Furnace Co., LTD), where each zone is 20 cm in length. The base pressure in the system amounts to 10^{-2} mbar, and the deposition pressure is maintained by an automated pressure regulating system. A schematic of the CVD system is given in the Supporting Information (Figure S1a). For the deposition of the lead iodide (PbI_2) thin films (step 1), about 150 mg of lead(II) iodide powder (99%, Sigma-Aldrich) in a ceramic boat was placed in the center of the first zone, and the Corning glass substrates were placed downstream, 15 cm away from PbI_2 source mounted on a ceramic substrate holder. The first zone was subsequently ramped at 10 °C/min up to a nominal temperature of 380 °C, which is above the known sublimation temperature of PbI_2. The temperature of the Corning glass substrate (15 cm downstream from the source) amounted to 145 °C. To transport the PbI_2 vapors toward the substrates, a nitrogen gas (N_2) flow rate of 100 sccm was maintained at a deposition pressure of 300 mbar. The deposition time amounted to 40 min for the complete consumption of the PbI_2 powder. Thereafter, the N_2 flow was interrupted, and the samples were allowed to cool to room temperature. A yellowish, compact PbI_2 thin film was produced, and no post-treatment was performed on the PbI_2 thin films (Figure S1b).

The perovskite conversion of the PbI_2 thin films (step 2) was performed in the aforementioned CVD system. About 200 mg of methylammonium iodide (MAI) (Dyesol) salt was placed in a fresh ceramic boat at also at the center of the first zone and PbI_2 thin films placed 8 cm downstream from the MAI. The temperature of the MAI boat was subsequently ramped at 10 °C/min up to a nominal temperature of 180 °C. The temperature of the PbI_2/glass substrate (8 cm downstream from the source) amounted to 130 °C. The MAI vapors were transported toward the PbI_2 thin films by a N_2 flow of 100 sccm at a constant pressure of 50 mbar. To investigate the perovskite conversion process, the conversion times for the $MAPbI_3$ samples were fixed to 15, 30, 60, 90, and 120 min. Figure S1b displays photographs of the PbI_2 thin film and the converted $MAPbI_3$ samples after various conversion times.

Perovskite Solar Cell Fabrication. The device fabrication was done under ambient conditions (temperature and humidity) in air. All chemicals used here were purchased from Sigma-Aldrich and used as bought. Fluorine-doped tin oxide (FTO)-coated glass substrates (10 ohm/sq) were cut into 1.5 cm × 2 cm sections and etched with Zn powder and 2 M hydrochloric acid (HCl). These samples were sequentially cleaned with Hellmanex detergent (2%) and isopropanol in an ultrasonic bath followed by a thorough rinsing in hot deionized water and finally cleaned with UV ozone for 10 min. A 365 μL aliquot of titanium isopropoxide was added into 2.5 mL of ethanol, and 35 μL of HCl (2 M) also added into 2.5 mL of ethanol, mixed to form 5 mL solution, and stirred for an hour. The prepared solution was spin-coated on the etched FTO substrates at 2000 rpm for 30 s to obtain a titanium containing film followed by 4000 rpm spin coating as a second coat, also for 30 s, to fill any voids left during the first spin coating step. The samples were dried on a hot plate at 150 °C for 5 min and then annealed at 500 °C for 30 min by using a tube furnace at atmosphere to form a compact (c-)TiO_2 film. The fully converted (90 min) perovskite film was employed as the absorber layer onto the c-TiO_2 layer. To finalize the device a hole transport layer (HTL) was spin-coated on top of the perovskite film at spin speed of 2000 rpm for 30 s. The HTL solution was prepared by dissolving 80 mg of Spiro-MeOTAD in 1 mL of chlorobenzene, to which 40 μL of 4-*tert*-butylpyridine (tBP) and 25 μL of lithium bis(trifluoromethanesulfonyl)imide (LITSFI) solution (52 mg of LITSFI in 100 μL of acetonitrile) were added and stirred for 30 min. Finally, 100 nm of silver electrode was deposited by thermal evaporation at a deposition pressure of 10^{-5} mbar through a shadow mask with device active area of 0.05 cm^2.

Characterization. The phase composition and the crystal structure were identified by X-ray diffraction (XRD) using a PANalytical Empyrean X-ray diffractometer with Cu Kα radiation (1.54 Å) at an acceleration voltage of 45 kV and current of 40 mA over the 2θ range of 5°−50° with a scan step of 0.02°. The morphology of the thin films was investigated by using a Zeiss Cross Beam 540 focused ion beam scanning electron microscope (FIBSEM) operated at acceleration voltages of 1−3 kV and equipped with energy dispersive X-ray spectroscopy (EDS) for elemental composition. X-ray photoelectron spectroscopy (XPS) was performed on a Thermo Scientific ESCALAB 250 surface and depth analysis system equipped with a monochromatic Al Kα X-ray (1486.7 eV) source. Optical transmission spectra were measured from 250 to 1000 nm with a spectral resolution of 0.5 nm by using an Ocean Optics UV−vis spectrophotometer. Current density−voltage ($J-V$) characteristics were recorded with a Keithley 2420 source meter under illumination of 100 mW/cm^2, AM1.5, by a solar simulator (Sciencetech Inc.) in air. The cells were illuminated for 15 s before measurements with $J-V$ curves recorded in forward scan (−0.2 to 1 V) and reverse scan (1 to −0.2 V) with a step voltage of 12 mV.

https://dx.doi.org/10.1021/acsaem.9b01925
ACS Appl. Energy Mater. 2020, 3, 2350−2359

■ ASSOCIATED CONTENT

Supporting Information

The Supporting Information is available free of charge at https://pubs.acs.org/doi/10.1021/acsaem.9b01925.

Schematic illustration of the home-built chemical vapor deposition system; photographs of the deposited films; optical, AFM, and SEM micrographs of the thin films; XPS full survey and high-resolution spectra of thin films; absorbance, absorption coefficient, refractive index, and optical band gap extrapolation of the thin films; $J-V$ curves measured at different days for reverse and forward scans; evolution of solar cell device performance measured for 21 days in reverse and forward scans (PDF)

■ AUTHOR INFORMATION

Corresponding Author

Christopher J. Arendse − *Department of Physics and Astronomy, University of the Western Cape, Bellville 7535, South Africa; Department of Physics and Astronomy, University of Missouri, Columbia, Missouri 65211, United States;* orcid.org/0000-0002-8505-5320; Email: cjarendse@uwc.ac.za

Authors

Siphelo Ngqoloda − *Department of Physics and Astronomy, University of the Western Cape, Bellville 7535, South Africa*

Theophillus F. Muller − *Department of Physics and Astronomy, University of the Western Cape, Bellville 7535, South Africa;* orcid.org/0000-0003-0182-459X

Paul F. Miceli − *Department of Physics and Astronomy, University of the Western Cape, Bellville 7535, South Africa; Department of Physics and Astronomy, University of Missouri, Columbia, Missouri 65211, United States*

Suchismita Guha − *Department of Physics and Astronomy, University of the Western Cape, Bellville 7535, South Africa; Department of Physics and Astronomy, University of Missouri, Columbia, Missouri 65211, United States;* orcid.org/0000-0002-6269-2298

Louise Mostert − *Materials Characterization, National Metrology Institute of South Africa, Pretoria 0040, South Africa*

Clive J. Oliphant − *Department of Physics and Astronomy, University of the Western Cape, Bellville 7535, South Africa; Materials Characterization, National Metrology Institute of South Africa, Pretoria 0040, South Africa*

Complete contact information is available at: https://pubs.acs.org/10.1021/acsaem.9b01925

Notes

The authors declare no competing financial interest.

■ ACKNOWLEDGMENTS

Financial support is gratefully acknowledged from the National Research Foundation (Grants 103621, 92520, and 93212), the University of the Western Cape, the National Metrology Institute of South Africa, and the University of Missouri−University of Western Cape Linkage Program. S.G. was supported by the National Science Foundation Grant DMR-1807263.

■ REFERENCES

(1) Djurišić, A. B.; Liu, F. Z.; Tam, H. W.; Wong, M. K.; Ng, A.; Surya, C.; Chen, W.; He, Z. B. Perovskite Solar Cells - an Overview of Critical Issues. *Prog. Quantum Electron.* **2017**, *53*, 1−37.

(2) Senanayak, S. P.; Yang, B.; Thomas, T. H.; Giesbrecht, N.; Huang, W.; Gann, E.; Nair, B.; Goedel, K.; Guha, S.; Moya, X.; McNeill, C. R.; Docampo, P.; Sadhanala, A.; Friend, R. H.; Sirringhaus, H. Understanding Charge Transport in Lead Iodide Perovskite Thin-Film Field-Effect Transistors. *Sci. Adv.* **2017**, *3*, e1601935.

(3) Wang, R.; Mujahid, M.; Duan, Y.; Wang, Z.-K.; Xue, J.; Yang, Y. A Review of Perovskites Solar Cell Stability. *Adv. Funct. Mater.* **2019**, *29*, 1808843.

(4) Kojima, A.; Teshima, K.; Shirai, Y.; Miyasaka, T. Organometal Halide Perovskites as Visible-Light Sensitizers for Photovoltaic Cells. *J. Am. Chem. Soc.* **2009**, *131*, 6050−6051.

(5) Lee, M. M.; Teuscher, J.; Miyasaka, T.; Murakami, T. N.; Snaith, H. J. Efficient Hybrid Solar Cells Based on Meso-Superstructured Organometal Halide Perovskites. *Science* **2012**, *338*, 643−647.

(6) https://www.nrel.gov/pv/cell-efficiency.html, NREL, 2020.

(7) Ono, L. K.; Leyden, M. R.; Wang, S.; Qi, Y. Organometal Halide Perovskite Thin Films and Solar Cells by Vapor Deposition. *J. Mater. Chem. A* **2016**, *4*, 6693−6713.

(8) Xi, H.; Tang, S.; Ma, X.; Chang, J.; Chen, D.; Lin, Z.; Zhong, P.; Wang, H.; Zhang, C. Performance Enhancement of Planar Heterojunction Perovskite Solar Cells through Tuning the Doping Properties of Hole-Transporting Materials. *ACS Omega* **2017**, *2*, 326−336.

(9) Kato, Y.; Ono, L. K.; Lee, M. V.; Wang, S.; Raga, S. R.; Qi, Y. Silver Iodide Formation in Methyl Ammonium Lead Iodide Perovskite Solar Cells with Silver Top Electrodes. *Adv. Mater. Interfaces* **2015**, *2*, 1500195.

(10) Chen, Q.; Zhou, H.; Hong, Z.; Luo, S.; Duan, H.-S.; Wang, H.-H.; Liu, Y.; Li, G.; Yang, Y. Planar Heterojunction Perovskite Solar Cells Via Vapor-Assisted Solution Process. *J. Am. Chem. Soc.* **2014**, *136*, 622−625.

(11) Sheng, R.; Ho-Baillie, A.; Huang, S.; Chen, S.; Wen, X.; Hao, X.; Green, M. A. Methylammonium Lead Bromide Perovskite-Based Solar Cells by Vapor-Assisted Deposition. *J. Phys. Chem. C* **2015**, *119*, 3545−3549.

(12) Chen, C.-W.; Kang, H.-W.; Hsiao, S.-Y.; Yang, P.-F.; Chiang, K.-M.; Lin, H.-W. Efficient and Uniform Planar-Type Perovskite Solar Cells by Simple Sequential Vacuum Deposition. *Adv. Mater.* **2014**, *26*, 6647−6652.

(13) Liu, M.; Johnston, M. B.; Snaith, H. J. Efficient Planar Heterojunction Perovskite Solar Cells by Vapour Deposition. *Nature* **2013**, *501*, 395−398.

(14) Ha, S. T.; Liu, X.; Zhang, Q.; Giovanni, D.; Sum, T. C.; Xiong, Q. Synthesis of Organic−Inorganic Lead Halide Perovskite Nanoplatelets: Towards High-Performance Perovskite Solar Cells and Optoelectronic Devices. *Adv. Opt. Mater.* **2014**, *2*, 838−844.

(15) Luo, P.; Liu, Z.; Xia, W.; Yuan, C.; Cheng, J.; Lu, Y. Uniform, Stable, and Efficient Planar-Heterojunction Perovskite Solar Cells by Facile Low-Pressure Chemical Vapor Deposition under Fully Open-Air Conditions. *ACS Appl. Mater. Interfaces* **2015**, *7*, 2708−2714.

(16) Tavakoli, M. M.; Gu, L.; Gao, Y.; Reckmeier, C.; He, J.; Rogach, A. L.; Yao, Y.; Fan, Z. Fabrication of Efficient Planar Perovskite Solar Cells Using a One-Step Chemical Vapor Deposition Method. *Sci. Rep.* **2015**, *5*, 14083.

(17) Leyden, M. R.; Ono, L. K.; Raga, S. R.; Kato, Y.; Wang, S.; Qi, Y. High Performance Perovskite Solar Cells by Hybrid Chemical Vapor Deposition. *J. Mater. Chem. A* **2014**, *2*, 18742−18745.

(18) Leyden, M. R.; Jiang, Y.; Qi, Y. Chemical Vapor Deposition Grown Formamidinium Perovskite Solar Modules with High Steady State Power and Thermal Stability. *J. Mater. Chem. A* **2016**, *4*, 13125−13132.

(19) Shen, P.-S.; Chen, J.-S.; Chiang, Y.-H.; Li, M.-H.; Guo, T.-F.; Chen, P. Low-Pressure Hybrid Chemical Vapor Growth for Efficient

Perovskite Solar Cells and Large-Area Module. *Adv. Mater. Interfaces* **2016**, *3*, 1500849.
(20) Wang, B.; Chen, T. Exceptionally Stable $CH_3NH_3PbI_3$ Films in Moderate Humid Environmental Condition. *Adv. Sci.* **2016**, *3*, 1500262.
(21) Peng, Y.; Jing, G.; Cui, T. A Hybrid Physical−Chemical Deposition Process at Ultra-Low Temperatures for High-Performance Perovskite Solar Cells. *J. Mater. Chem. A* **2015**, *3*, 12436−12442.
(22) Ioakeimidis, A.; Christodoulou, C.; Lux-Steiner, M.; Fostiropoulos, K. Effect of PbI_2 Deposition Rate on Two-Step Pvd/Cvd All-Vacuum Prepared Perovskite. *J. Solid State Chem.* **2016**, *244*, 20−24.
(23) Shen, P.-S.; Chiang, Y.-H.; Li, M.-H.; Guo, T.-F.; Chen, P. Research Update: Hybrid Organic-Inorganic Perovskite (HOIP) Thin Films and Solar Cells by Vapor Phase Reaction. *APL Mater.* **2016**, *4*, 091509.
(24) Jiang, Y.; Leyden, M. R.; Qiu, L.; Wang, S.; Ono, L. K.; Wu, Z.; Juarez-Perez, E. J.; Qi, Y. Combination of Hybrid Cvd and Cation Exchange for Upscaling Cs-Substituted Mixed Cation Perovskite Solar Cells with High Efficiency and Stability. *Adv. Funct. Mater.* **2018**, *28*, 1703835.
(25) Wei, X.; Peng, Y.; Jing, G.; Cui, T. Planar Structured Perovskite Solar Cells by Hybrid Physical Chemical Vapor Deposition with Optimized Perovskite Film Thickness. *Jpn. J. Appl. Phys.* **2018**, *57*, 052301.
(26) Tran, V.-D.; Pammi, S. V. N.; Dao, V.-D.; Choi, H.-S.; Yoon, S.-G. Chemical Vapor Deposition in Fabrication of Robust and Highly Efficient Perovskite Solar Cells Based on Single-Walled Carbon Nanotubes Counter Electrodes. *J. Alloys Compd.* **2018**, *747*, 703−711.
(27) Yin, J.; Qu, H.; Cao, J.; Tai, H.; Li, J.; Zheng, N. Vapor-Assisted Crystallization Control toward High Performance Perovskite Photovoltaics with over 18% Efficiency in the Ambient Atmosphere. *J. Mater. Chem. A* **2016**, *4*, 13203−13210.
(28) Swartwout, R.; Hoerantner, M. T.; Bulović, V. Scalable Deposition Methods for Large-Area Production of Perovskite Thin Films. *Energy Environ. Sci.* **2019**, *2*, 119−145.
(29) Luo, P.; Zhou, S.; Xia, W.; Cheng, J.; Xu, C.; Lu, Y. Chemical Vapor Deposition of Perovskites for Photovoltaic Application. *Adv. Mater. Interfaces* **2017**, *4*, 1600970.
(30) Bai, S.; Da, P.; Li, C.; Wang, Z.; Yuan, Z.; Fu, F.; Kawecki, M.; Liu, X.; Sakai, N.; Wang, J. T.-W.; Huettner, S.; Buecheler, S.; Fahlman, M.; Gao, F.; Snaith, H. J. Planar Perovskite Solar Cells with Long-Term Stability Using Ionic Liquid Additives. *Nature* **2019**, *571*, 245−250.
(31) Pammi, S. V. N.; Lee, H.-W.; Eom, J.-H.; Yoon, S.-G. Predominant Stable $MAPbI_3$ Films Deposited Via Chemical Vapor Deposition: Stability Studies in Illuminated and Darkened States Coupled with Temperature under an Open-Air Atmosphere. *ACS Appl. Energy Mater.* **2018**, *1*, 3301−3312.
(32) Shallcross, R. C.; Olthof, S.; Meerholz, K.; Armstrong, N. R. Impact of Titanium Dioxide Surface Defects on the Interfacial Composition and Energetics of Evaporated Perovskite Active Layers. *ACS Appl. Mater. Interfaces* **2019**, *11*, 32500−32508.
(33) Hoerantner, M. T.; Wassweiler, E. L.; Zhang, H.; Panda, A.; Nasilowski, M.; Osherov, A.; Swartwout, R.; Driscoll, A. E.; Moody, N. S.; Bawendi, M. G.; Jensen, K. F.; Bulović, V. High-Speed Vapor Transport Deposition of Perovskite Thin Films. *ACS Appl. Mater. Interfaces* **2019**, *11*, 32928−32936.
(34) Cao, H.; Li, J.; Dong, Z.; Su, J.; Chang, J.; Zhao, Q.; Li, Z.; Yang, L.; Yin, S. Reducing Defects in Perovskite Solar Cells with White Light Illumination-Assisted Synthesis. *ACS Energy Lett.* **2019**, *4*, 2821−2829.
(35) Li, J.; Cao, H.; Wang, X.; Zhu, H.; Dong, Z.; Yang, L.; Yin, S. Vapor Exchange Deposition of an Air-Stable Lead Iodide Adduct on 19% Efficient 1.8 cm^2 Perovskite Solar Cells. *ACS Appl. Energy Mater.* **2019**, *2*, 2506−2514.
(36) Li, M.-H.; Yeh, H.-H.; Chiang, Y.-H.; Jeng, U.-S.; Su, C.-J.; Shiu, H.-W.; Hsu, Y.-J.; Kosugi, N.; Ohigashi, T.; Chen, Y.-A.; Shen, P.-S.; Chen, P.; Guo, T.-F. Highly Efficient 2d/3d Hybrid Perovskite Solar Cells Via Low-Pressure Vapor-Assisted Solution Process. *Adv. Mater.* **2018**, *30*, 1801401.
(37) Sun, H.; Zhu, X.; Yang, D.; Yang, J.; Gao, X.; Li, X. Morphological and Structural Evolution During Thermally Physical Vapor Phase Growth of PbI_2 Polycrystalline Thin Films. *J. Cryst. Growth* **2014**, *405*, 29−34.
(38) Schieber, M.; Zamoshchik, N.; Khakhan, O.; Zuck, A. Structural Changes During Vapor-Phase Deposition of Polycrystalline-PbI_2 Films. *J. Cryst. Growth* **2008**, *310*, 3168−3173.
(39) Fu, F.; Kranz, L.; Yoon, S.; Löckinger, J.; Jäger, T.; Perrenoud, J.; Feurer, T.; Gretener, C.; Buecheler, S.; Tiwari, A. N. Controlled Growth of PbI_2 Nanoplates for Rapid Preparation of $CH_3NH_3PbI_3$ in Planar Perovskite Solar Cells. *Phys. Status Solidi A* **2015**, *212*, 2708−2717.
(40) Kim, H.-S.; Im, S. H.; Park, N.-G. Organolead Halide Perovskite: New Horizons in Solar Cell Research. *J. Phys. Chem. C* **2014**, *118*, 5615−5625.
(41) Baikie, T.; Fang, Y.; Kadro, J. M.; Schreyer, M.; Wei, F.; Mhaisalkar, S. G.; Graetzel, M.; White, T. J. Synthesis and Crystal Chemistry of the Hybrid Perovskite $(CH_3NH_3)PbI_3$ for Solid-State Sensitised Solar Cell Applications. *J. Mater. Chem. A* **2013**, *1*, 5628−5641.
(42) Liu, X.; Xia, X.; Cai, Q.; Cai, F.; Yang, L.; Yan, Y.; Wang, T. Efficient Planar Heterojunction Perovskite Solar Cells with Weak Hysteresis Fabricated Via Bar Coating. *Sol. Energy Mater. Sol. Cells* **2017**, *159*, 412−417.
(43) Zhang, W.; Pathak, S.; Sakai, N.; Stergiopoulos, T.; Nayak, P. K.; Noel, N. K.; Haghighirad, A. A.; Burlakov, V. M.; deQuilettes, D. W.; Sadhanala, A.; Li, W.; Wang, L.; Ginger, D. S.; Friend, R. H.; Snaith, H. J. Enhanced Optoelectronic Quality of Perovskite Thin Films with Hypophosphorous Acid for Planar Heterojunction Solar Cells. *Nat. Commun.* **2015**, *6*, 10030.
(44) Song, Z.; Watthage, S. C.; Phillips, A. B.; Tompkins, B. L.; Ellingson, R. J.; Heben, M. J. Impact of Processing Temperature and Composition on the Formation of Methylammonium Lead Iodide Perovskites. *Chem. Mater.* **2015**, *27*, 4612−4619.
(45) Jain, S. M.; Philippe, B.; Johansson, E. M. J.; Park, B.-w.; Rensmo, H.; Edvinsson, T.; Boschloo, G. Vapor Phase Conversion of PbI_2 to $CH_3NH_3PbI_3$: Spectroscopic Evidence for Formation of an Intermediate Phase. *J. Mater. Chem. A* **2016**, *4*, 2630−2642.
(46) Liu, D.; Gangishetty, M. K.; Kelly, T. L. Effect of $CH_3NH_3PbI_3$ Thickness on Device Efficiency in Planar Heterojunction Perovskite Solar Cells. *J. Mater. Chem. A* **2014**, *2*, 19873−19881.
(47) Green, M. A.; Jiang, Y.; Soufiani, A. M.; Ho-Baillie, A. Optical Properties of Photovoltaic Organic−Inorganic Lead Halide Perovskites. *J. Phys. Chem. Lett.* **2015**, *6*, 4774−4785.
(48) Lin, Q.; Armin, A.; Nagiri, R. C. R.; Burn, P. L.; Meredith, P. Electro-Optics of Perovskite Solar Cells. *Nat. Photonics* **2015**, *9*, 106−112.
(49) Tombe, S.; Adam, G.; Heilbrunner, H.; Apaydin, D. H.; Ulbricht, C.; Sariciftci, N. S.; Arendse, C. J.; Iwuoha, E.; Scharber, M. C. Optical and Electronic Properties of Mixed Halide (X = I, Cl, Br) Methylammonium Lead Perovskite Solar Cells. *J. Mater. Chem. C* **2017**, *5*, 1714−1723.
(50) Ahn, N.; Kwak, K.; Jang, M. S.; Yoon, H.; Lee, B. Y.; Lee, J.-K.; Pikhitsa, P. V.; Byun, J.; Choi, M. Trapped Charge-Driven Degradation of Perovskite Solar Cells. *Nat. Commun.* **2016**, *7*, 13422.
(51) Jena, A. K.; Chen, H.-W.; Kogo, A.; Sanehira, Y.; Ikegami, M.; Miyasaka, T. The Interface between FTO and the TiO_2 Compact Layer Can Be One of the Origins to Hysteresis in Planar Heterojunction Perovskite Solar Cells. *ACS Appl. Mater. Interfaces* **2015**, *7*, 9817−9823.
(52) Yin, G.; Ma, J.; Jiang, H.; Li, J.; Yang, D.; Gao, F.; Zeng, J.; Liu, Z.; Liu, S. F. Enhancing Efficiency and Stability of Perovskite Solar Cells through Nb-Doping of TiO_2 at Low Temperature. *ACS Appl. Mater. Interfaces* **2017**, *9*, 10752−10758.
(53) Liu, D.; Li, S.; Zhang, P.; Wang, Y.; Zhang, R.; Sarvari, H.; Wang, F.; Wu, J.; Wang, Z.; Chen, Z. D. Efficient Planar

https://dx.doi.org/10.1021/acsaem.9b01925
ACS Appl. Energy Mater. 2020, 3, 2350−2359

Heterojunction Perovskite Solar Cells with Li-Doped Compact TiO_2 Layer. *Nano Energy* **2017**, *31*, 462−468.
(54) Guo, X.; Zhang, B.; Lin, Z.; Ma, J.; Su, J.; Zhu, W.; Zhang, C.; Zhang, J.; Chang, J.; Hao, Y. Interface Engineering of TiO_2/Perovskite Interface Via Fullerene Derivatives for High Performance Planar Perovskite Solar Cells. *Org. Electron.* **2018**, *62*, 459−467.

https://dx.doi.org/10.1021/acsaem.9b01925
ACS Appl. Energy Mater. 2020, 3, 2350−2359